


Structure and electron dynamics of planetary states of Sr below the Sr^+ $7d$ and $8p$ thresholds

M. Génévriez ^{*}*Laboratory of Physical Chemistry, ETH Zürich, CH-8093 Zürich, Switzerland*

C. Rosen and U. Eichmann

Max-Born-Institute, 12489 Berlin, Germany

(Received 7 May 2021; accepted 7 July 2021; published 26 July 2021)

In a combined experimental and theoretical study we investigate the $7dnl$ and $8pnl$ ($n \geq 11$, $l = 9-12$) doubly excited planetary states of Sr. The experimental spectrum was obtained using a five-photon resonant excitation scheme. The method of configuration interaction with exterior complex scaling was used to compute the energy-level structure and dynamics of the two highly excited electrons from first principles. Good quantitative agreement was obtained with the spectra we recorded, and the theoretical calculations shed light on their complex structure and the signatures of electron correlations therein. The two-electron probability densities we calculated reveal the strongly correlated angular motion of the two electrons in the $7dnl$ and $8pnl$ planetary states, and confirm quantitatively the predictions of the frozen-planet approximation describing electron dynamics as the polarization of the fast inner electron by the electric field of the outer “frozen” electron.

DOI: [10.1103/PhysRevA.104.012812](https://doi.org/10.1103/PhysRevA.104.012812)

I. INTRODUCTION

Electronic states of atoms and molecules in which two electrons are excited to Rydberg states, the so-called double Rydberg states, have been extensively used to study in great detail many aspects of the three-body quantum-mechanical problem [1,2]. Because Rydberg electrons spend most of their time far away from the residual doubly charged ion core, correlations between the two Rydberg electrons evolving in the Coulomb field of the core are magnified compared to residual interactions with the core electrons. Combined with the large density of accessible states, this makes electronic motion in double-Rydberg states rich and complex [2–4] and may give rise to strongly correlated dynamics in which each of the three Coulomb interactions plays an essential role, as is the case for the frozen-planet states theoretically predicted in the helium atom [5].

Strontium atoms, along with the other alkaline-earth metals, are well suited to study double Rydberg states experimentally because they possess only two valence electrons which can be photoexcited with conventional visible and ultraviolet lasers. Asymmetric double Rydberg states, in which the (approximate) principal quantum numbers associated with the two electrons are significantly different ($n_1 \ll n_2$), have been experimentally studied and characterized in Sr for a broad range of angular momentum values [6–14]. Because they lie above the first ionization threshold, double-Rydberg states can decay rapidly by autoionization. Planetary configurations [15], in which autoionization is suppressed and the two electrons orbit the nucleus in a solar-system-like manner, have been obtained [4,9,16–18]. In addition to their fundamental role in the development of multichannel theories [1,19], core-excited Rydberg states, in which one of the two electrons is in

a low-lying excited state of the ion core, recently gained particular interest in the context of quantum optics and quantum simulation [20–25]. The possibility to manipulate the valence electron of the residual ion core within the Rydberg electron orbit offers a number of exciting perspectives to, e.g., detect [23], image [20], or trap [26] Rydberg atoms.

As the degree of excitation of both electrons increases (n_1 and n_2 large), spectra associated with double-Rydberg series becoming increasingly complex because the density of states increases and Rydberg-series interactions become ubiquitous. Several electrostatic models were developed to qualitatively describe the energy-level structure and two-electron wave functions of the high angular momentum double-Rydberg states measured in alkaline-earth-metal atoms [9,10,17,27–31]. They describe the correlations between the two Rydberg electrons of such systems as the polarization of the fast inner electron by the electric field of the slow outer electron, the so-called frozen-planet approximation [9]. However, in contrast with the numerous studies carried out for the helium atom [2,32–40], no quantitative theoretical information is available for alkaline-earth-metal atoms to date, in particular concerning the complex photoexcitation spectra recorded in the experiments. With one exception [41], no attempt was made to calculate doubly excited Rydberg states of Sr from first principles. With the development of the method of configuration interaction with exterior complex scaling (CI-ECS), accurate calculations that treat the interaction between the two electrons to all orders everywhere are now feasible [42]. It offers the possibility to (i) quantitatively analyze and assign experimental spectra, (ii) assess the validity of the aforementioned models, and (iii) investigate correlated electron dynamics in regions of phase space where these models are not applicable.

We present a joint experimental and theoretical study of planetary states of Sr located below the Sr^+ ($7d$) and Sr^+ ($8p$)

^{*}matthieu.genevriez@phys.chem.ethz.ch

limits. Experimental photoexcitation spectra were recorded from $5d_{5/2}16(l_2 \sim 10)$ states prepared by isolated-core excitation (ICE) [7], as presented in Sec. II. The large-scale CI-ECS approach we then used to calculate doubly excited Rydberg states of Sr is described in Sec. III, along with the procedure employed to simulate experimental spectra. Experimental and theoretical spectra are presented and analyzed in Sec. IV. In the light of their good mutual agreement, reliable electronic densities derived from the CI-ECS calculations are then used to investigate electronic correlations and describe the two-electron collective motion in the planetary states under scrutiny. These results are further discussed in Sec. V and analyzed in the light of existing models and theories describing planetary states.

II. EXPERIMENT

The experimental setup and the resonant multiphoton laser excitation scheme used in the present experiment are identical to the ones described in Ref. [11]. Strontium atoms in the ground state emanating from a resistively heated oven are excited in the presence of a constant electric field to a $5s16k$ ($m = 0$) Stark state by two excimer-laser-pumped dye lasers, which are parallel linearly polarized. m is the magnetic quantum number and k indicates a particular Stark state. After the excitation, the electric field is switched off adiabatically within $1.5 \mu\text{s}$ and the Stark state is ideally converted into a single angular momentum eigenstate $5s16(l_2 \sim 10)$ [43]. As will be discussed in Sec. III B nonadiabatic effects effectively result in an admixture of neighboring angular momentum states. Applying the ICE technique, Sr atoms in the $5s16l_2$ state are further excited via the $5p_{3/2}16l_2$ to the $5d_{5/2}16l_2$ state by another two dye lasers pumped by a second excimer laser. The two dye lasers are also parallel linearly polarized to ensure $\Delta m = 0$ transitions only. Due to the high angular momentum involved, autoionization of the intermediate states is largely suppressed. A fifth dye laser is scanned in the energy range of the $7d_{5/2}n'l'$ and $8p_{3/2}n''l''$ series. The doubly excited atoms either autoionize or are directly photoionized by the fifth dye laser. As detailed in Sec. III B the resulting excited Sr^+ ions are further photoionized, or ionized by a strong static electric-field pulse to yield Sr^{2+} ions, which are detected in our experiment. The Sr^{2+} spectrum displayed in Fig. 1 is obtained by recording the Sr^{2+} ion yield as a function of the wavelength of the fifth laser. Calibration of the wavelength has been achieved by means of an optogalvanic Ar spectrum and using the known transition energies of Sr^+ ionic lines which appear in the spectra. In our time-of-flight spectrometer the static pulsed field serves also to sweep the Sr^{2+} ions to the multichannel plate ion detector.

III. THEORY

A. Configuration interaction with exterior complex scaling

The CI-ECS method [42,44] was used to calculate the energies, widths, and complex-scaled wave functions of the relevant Sr doubly excited states, and to determine the photoionization cross sections and electronic densities presented in Sec. IV. We sketch below the parts of the method relevant

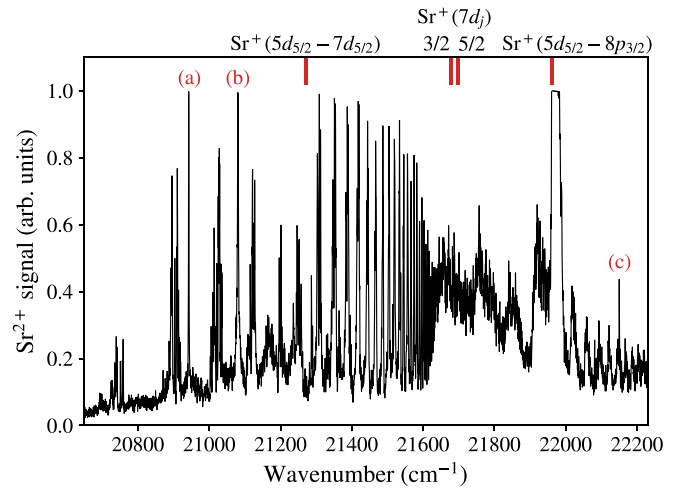


FIG. 1. Experimental Sr^{2+} spectrum recorded from $[5d_{5/2}16(l_2)_{j_2}]_J$ states. The vertical lines on the top horizontal axis indicate the wave numbers of the $\text{Sr}^+(5d_{5/2} - 7d_{5/2})$ dipole-forbidden isolated-core resonance, of the $\text{Sr}^+(7d_{j=3/2,5/2})$ ionization thresholds, and of the $\text{Sr}^+(5d_{5/2} - 8p_{3/2})$ isolated-core resonance, respectively. The labels (a)–(c) indicate the wave numbers of the one-photon ionic transitions $\text{Sr}^+(6s_{1/2} - 7p_{1/2})$ and $\text{Sr}^+(6s_{1/2} - 7p_{3/2})$, and of the two-photon ionic transition $\text{Sr}^+(5p_{3/2} - 7p_{3/2})$.

to the present paper. Atomic units are used throughout the rest of the section unless stated otherwise.

Within the CI-ECS approach, the two valence electrons of Sr are explicitly treated whereas the influence of the electrons of the closed-shell Sr^{2+} core is accounted for by an ℓ -dependent empirical model potential $V_\ell(r)$, the parameters of which were adjusted to reproduce the energies of the Sr^+ ion [1]. Singly and doubly excited Rydberg states of Sr are thus described by the effective two-electron Hamiltonian

$$\hat{H}(\mathbf{r}_1, \mathbf{r}_2) = -\frac{1}{2}\nabla_1^2 - \frac{1}{2}\nabla_2^2 + V_{l_1}(r_1) + V_{l_2}(r_2) + \frac{1}{r_{12}} + V_{s_1l_1j_1}^{\text{SO}}(r_1) + V_{s_2l_2j_2}^{\text{SO}}(r_2) + V_{\text{pol}}^{(2)}(\mathbf{r}_1, \mathbf{r}_2). \quad (1)$$

The two electrons have positions with respect to the nucleus given by \mathbf{r}_1 and \mathbf{r}_2 , and are described by the independent-electron orbital-, spin-, and total angular momentum quantum numbers ℓ , s , and j . The distance between the two electrons is given by $r_{12} = |\mathbf{r}_1 - \mathbf{r}_2|$. $V_{s\ell j}^{\text{SO}}(r)$ is the spin-orbit interaction between a valence electron and the screened nucleus and $V_{\text{pol}}^{(2)}(\mathbf{r}_1, \mathbf{r}_2)$ represents bielectronic core polarization. Their expressions are given, e.g., in Ref. [42].

The time-independent Schrödinger equation associated with the Hamiltonian in Eq. (1) is solved, in a CI manner, using a large basis of two-electron functions built from antisymmetrized products of two one-electron spin orbitals of the Sr^+ ion. Continuum states and resonances are accounted for with exterior complex scaling [45], following which the radial coordinate of each electron is rotated into the complex plane after a certain ECS radius r_0 :

$$r \rightarrow \begin{cases} r & \text{if } r < r_0, \\ r_0 + (r - r_0)e^{i\theta} & \text{if } r \geq r_0. \end{cases} \quad (2)$$

TABLE I. FEM-DVR parameters used in the present calculations. The i th element spans radial distances from r_i to r_{i+1} and contains N_i grid points. The complex-scaling angle in this element is θ_i .

Element	$i = 1$	$i = 2$	$i = 3$
$[r_i, r_{i+1}]$	$[0, 10] a_0$	$[10, 150] a_0$	$[150, 1350] a_0$
N_i	70	60	80
θ_i	0	0	10°

As a result of ECS, the wave functions associated with resonances, which are not square integrable for real r values, become exponentially damped at large distances and the entire spectrum of bound and resonance radial wave functions can be represented by a discrete set of square-integrable functions.

In practice, the numerical one-electron radial functions used to build the two-electron CI wave functions are calculated along the ECS contour (2) using a finite-element discrete-variable-representation (FEM-DVR) method [46]. The calculation parameters are listed in Table I, and were chosen as described in Ref. [42]. Because, in a doubly excited state, only one of the two electrons can autoionize, the description of the second electron can be limited to a relatively compact set of bound one-electron orbitals of Sr^+ . This dramatically reduces the computational cost of solving the two-electron Schrödinger equation and makes it possible to treat accurately high-lying doubly excited states. In the present calculation, approximately 80 000 two-electron wave functions were built from (i) all spin orbitals with energies lower than the $\text{Sr}^+(11s)$ state and (ii) the complete set of spin orbitals associated with the 208 radial functions generated by the FEM-DVR calculation. The ECS radius $r_0 = 150 a_0$ is chosen such that the amplitudes of the radial functions of all states below the $\text{Sr}^+(11s)$ state are negligible at r_0 and beyond.

The complex-scaled two-electron Hamiltonian matrix is constructed using the large CI basis set and iteratively diagonalized in the relevant energy region with a Lanczos algorithm adapted to complex-symmetric matrices. Resonances associated with doubly excited states have complex eigenvectors and eigenvalues $E - i\Gamma/2$ giving the energies E and autoionization widths Γ of these states. We ensured that all relevant eigenvalues are converged to better than $0.5 \mu\text{hartree}$ (0.1 cm^{-1}) with respect to the number of grid points, the number of basis functions, and the complex-scaling angle.

The present calculations take into account the spin-orbit interaction for *both* electrons and are carried out using the jj coupling scheme. For the planetary states considered in the present paper, the spin-orbit interaction for the outer electron is very small and these states are commonly described using the jK coupling scheme. The transformation between the jj and jK coupling schemes is given by [47]

$$\begin{aligned} & \langle l_1 s_1 j_1 l_2 K (s_2 J) | l_1 s_1 j_1 l_2 s_2 j_2 J \rangle \\ &= (-1)^{j_1 + l_2 + s_2 + J} \sqrt{(2K+1)(2j_2+1)} \begin{Bmatrix} j_1 & l_2 & K \\ s_2 & J & j_2 \end{Bmatrix}. \end{aligned} \quad (3)$$

Total photoionization cross sections are calculated from the CI-ECS wave functions following the procedure of Rescigno

and McKoy [48] (see also Ref. [44]). The initial $\text{Sr}(5dn_2l_2)$ states are already autoionizing resonances lying above the first ionization threshold, but are treated as nondecaying states because of their low autoionization rates ($< 2 \times 10^{-9}$ a.u., i.e., lifetimes > 12 ns). Partial photoionization cross sections were calculated from the complex-scaled wave functions in the interior region ($r \leq r_0$) using an approach proposed by Carette *et al.* [49] and Mihelič [50]. We start from the driven Schrödinger equation,

$$[E_0 + \omega - \hat{H}(\mathbf{r}_1, \mathbf{r}_2)] |\Psi_1\rangle = \hat{D} |\Psi_0\rangle, \quad (4)$$

where $|\Psi_0\rangle$ is the wave function of the initial state with energy E_0 , ω is the photon angular frequency, and \hat{D} is the transition dipole operator. In the length gauge, used in the present paper, $\hat{D} = -\hat{\epsilon} \cdot (\mathbf{r}_1 + \mathbf{r}_2)$ where $\hat{\epsilon}$ is the polarization vector. The solution to Eq. (4) within the ECS framework is given by

$$|\Psi_1^\theta(\omega)\rangle = \sum_i |i^\theta\rangle \frac{\langle i^\theta | \hat{D} | \Psi_0 \rangle}{E_0 - E_i^\theta + \omega}, \quad (5)$$

where the summation runs over all ECS states $|i^\theta\rangle$ obtained by diagonalization of the complex-scaled two-electron Hamiltonian. Within the interior region ($r < r_0$), r is real and the wave function $|\Psi_1^\theta(\omega)\rangle$ is identical to the one without complex scaling. In the exterior region ($r \geq r_0$), r possesses an imaginary component such that the physical significance of $|\Psi_1^\theta(\omega)\rangle$ and its use to extract physically relevant information are significantly complicated. Therefore, partial cross sections are best obtained from $|\Psi_1^\theta(\omega)\rangle$ in the interior region just before r_0 , where we assume that it has already reached its asymptotic, Coulomb-type behavior. The function $|\Psi_1^\theta(\omega)\rangle$ is projected onto channel functions, which describe all but the radial motion of the photoelectron [1], yielding the radial function $P_\alpha(r_2; \omega)$. α stands for the quantum numbers $n_1, \ell_1, j_1, \ell_2, j_2, J$, and M which define a channel. Provided that r_0 is sufficiently large, $P_\alpha(r_2; \omega)$ can be represented for $r_2 \lesssim r_0$ by a linear combination of regular $F_{\ell_2}^E$ and irregular $G_{\ell_2}^E$ Coulomb functions:

$$P_\alpha(r_2; \omega) \sim A_\alpha(\omega) [F_{\ell_2}^E(-1/k, kr_2) + iG_{\ell_2}^E(-1/k, kr_2)], \quad (6)$$

where k and E are the photoelectron wave number and kinetic energy, respectively. The imaginary part of the right-hand side of Eq. (6) is fitted to $\text{Im}(P_\alpha)$, calculated from the CI-ECS wave function, in a linear least-squares fit with the amplitude $A(\omega)$ as a fit parameter. The partial cross section $\sigma_\alpha(\omega)$ at a photon angular frequency ω is then obtained from $A(\omega)$ using

$$\sigma_\alpha(\omega) = \frac{4\omega}{c} |A_\alpha(\omega)|^2. \quad (7)$$

Electronic correlations are investigated in their finest details by computing and analyzing the two-electron density (see, e.g., Refs. [33,51]). Because of ECS, the radial coordinates are rotated into the complex plane and the density cannot be straightforwardly computed from the complex-scaled two-electron wave function everywhere. Deducing the real- r wave function from its complex-rotated counterpart, a process known as backscaling, is possible for standard complex scaling ($r_0 = 0$) but suffers from severe numerical instabilities [52]. It is also unclear whether it can be extended to ECS. Instead, just as for computing partial photoionization

cross sections, we use the fact that for $r \leq r_0$ the radial coordinates are real and the functions $|i^\theta\rangle$ can be identified to their non-complex-scaled versions. Provided that we restrict ourselves to $r_1, r_2 \leq r_0$, the electronic density $\rho(\mathbf{r}_1, \mathbf{r}_2)$ can thus be calculated as usual. Integration of ρ over the Euler angles describing the orientation the electron-electron-nucleus triangle reduces the six-dimensional coordinate space to the three internal variables r_1, r_2 , and θ_{12} relevant for electron-electron correlations. θ_{12} is the interelectronic angle. The corresponding reduced two-electron density is calculated as

$$\rho_i(r_1, r_2, \cos \theta_{12}) = \langle i^\theta | \delta(r_1 - r'_1) \delta(r_2 - r'_2) \delta(\cos \theta_{12} - \cos \theta'_{12}) | i^\theta \rangle, \quad (8)$$

where $\delta(x)$ are Dirac delta functions. The expansion of $\delta(\cos \theta_{12} - \cos \theta'_{12})$ in terms of Legendre polynomials [53] is used for the calculations.

B. Simulation of experimental spectra

To reproduce the experimental spectra, the production dynamics of Sr^{2+} ions following excitation to doubly excited states must be elucidated. First, $[7d_{j_1} n_2 (l_2)_{j_2}]_J'$ or $[8p_{j_1} n_2 (l_2)_{j_2}]_J'$ states are photoexcited from $[5d_{5/2} 16(l_2)_{j_2}]_J$ states. Sr^{2+} ions are then detected following, predominantly, (i) autoionization and subsequent photoionization of the residual Sr^+ ion or (ii) photoionization of the core electron and subsequent field ionization of the Sr^+ ion in a Rydberg series. In process (i), the final state of the ion after autoionization is important. If it is energetically too low [$\leq \text{Sr}^+(6d_{5/2})$], the photon energy is not sufficient to photoionize the ion and Sr^{2+} ions are not detected. The photoionization cross section is also different for each Sr^+ final state. To assess the importance of these effects, we calculated partial photoionization cross sections to each Sr^+ final state and weighted them by the corresponding Sr^+ photoionization cross section. The corresponding spectra are very similar to the spectra obtained including all Sr^+ final states and without weighting (see red and black dotted lines in Fig. 3). Process (ii) was studied in detail by Rosen *et al.* [54]. Within the independent-electron approximation, the photoionization of the core electron is independent of the state of the Rydberg electron, and the field ionization of the Sr^+ Rydberg ion is also independent of the particular Rydberg state for sufficiently large field strengths.

The competition between processes (i) and (ii) depends in a complicated manner on the photoexcitation and autoionization dynamics. For the sake of simplicity, the theoretical spectra presented below are thus obtained from the total photoionization cross section of $[5d_{5/2} 16(l_2)_{j_2}]_J$ states unless stated otherwise.

The calculated photoionization cross sections are convolved by a Gaussian function with a full width at half maximum of 0.25 cm^{-1} to account for the finite laser bandwidth in the experiment. Theoretical spectra are obtained from the convolved cross section $\sigma_c(\omega)$ using

$$S(\omega) = \sum_i P_i \{ \ln [p_{\text{sat}} \sigma_c^i(\omega)] + \gamma - \text{Ei}[-p_{\text{sat}} \sigma_c^i(\omega)] \}, \quad (9)$$

where the coefficients P_i are the populations of the various $[5d_{5/2} 16(l_2)_{j_2}]_J$ initial states. γ is the Euler constant, $\text{Ei}(x)$ is the exponential integral function, and p_{sat} is a parameter adjusted to visually reproduce experimental spectra. This formula accounts exactly for both saturation and interaction-volume effects in the case of a Gaussian laser beam and a large atomic beam [55].

In the experiment, Sr atoms are prepared in $[5d_{5/2} 16(l_2)_{j_2}]_J$ states by ICE from bound singlet $5s16(l_2)$ Rydberg states, for which the LS coupling scheme is appropriate. In order to reproduce experimental spectra, the relative populations P_i of the various $[5d_{5/2} 16(l_2)_{j_2}]_J$ states must be estimated. A complete description of the preparation process using CI-ECS is computationally very demanding, since many eigenvalues and eigenvectors must be obtained from the large Hamiltonian matrix. Instead, we obtained an initial estimate using the ICE approximation [56] which relies on the independent-electron approximation. We treated the $5p_{3/2} 16l_2$ and $5d_{5/2} 16l_2$ weakly autoionizing doubly excited states as nondecaying states, i.e., we neglected the admixture of any continuum state, because as mentioned in Sec. III A their autoionization rates are small on the timescale of the experiment.

The initial $5s16(l_2)$ singlet states are projected onto the jj -coupled $[5s_{1/2} 16(l_2)_{j_2}]_{J'=l_2}$ states using standard angular momentum algebra [47]. The photoexcitation cross section from an initial $|n_1 l_1 j_1 n_2 l_2 j_2 JM\rangle$ state can be written, in the ICE approximation, as

$$\begin{aligned} \sigma_{\text{ICE}}(\omega) &= \frac{4\pi^2 \omega}{c} [J, J', j_1, j'_1] \begin{pmatrix} J' & 1 & J \\ -M' & q & M \end{pmatrix}^2 \begin{Bmatrix} j_2 & j'_1 & J' \\ 1 & J & j_1 \end{Bmatrix}^2 \begin{Bmatrix} l'_1 & 1/2 & j'_1 \\ j_1 & 1 & l_1 \end{Bmatrix}^2 \\ &\times |\langle n'_1 l'_1 j'_1 | \hat{\epsilon} \cdot \vec{r}_1 | n_1 l_1 j_1 \rangle|^2 |\langle n'_2 l_2 j_2 | n_2 l_2 j_2 \rangle|^2 A_{n'_1 l'_1 j'_1}^{l_2 j_2 J'}(\omega), \end{aligned} \quad (10)$$

where ω is the photon angular frequency and c is the speed of light. We use the standard notation $[j] = 2j + 1$. The first term on the second line is the square of the transition dipole moment for the excitation of the bare Sr^+ ion from the $n_1(l_1)_{j_1}$ state to the $n'_1(l'_1)_{j'_1}$ state. The second term describes the overlap between the initial and final Rydberg-state wave functions, and is well approximated by the sinc²-type function [56]

$$|\langle n'_2 l_2 j_2 | n_2 l_2 j_2 \rangle|^2 = \frac{4(n'_2 n_2)^4}{n_2^3 (n_2 + n'_2)^2} \text{sinc}^2(n'_2 - n_2). \quad (11)$$

The last term in Eq. (10) is the spectral density of the $n'_1(l'_1)_{j'_1}(l_2)_{j_2} J'$ doubly excited Rydberg series. In the absence of electron correlations, it is given by a series of narrow Lorentzian functions located at the energies of the Rydberg states. Because l_2 is large, the interaction between the two electrons during the preparation process is very small and, in particular, the quantum defects are assumed to be small ($n'_2 \simeq n_2$ and $E_{n'_2} \simeq E_{n_2}$). Consequently, the last two terms are nonzero only when ω corresponds to the

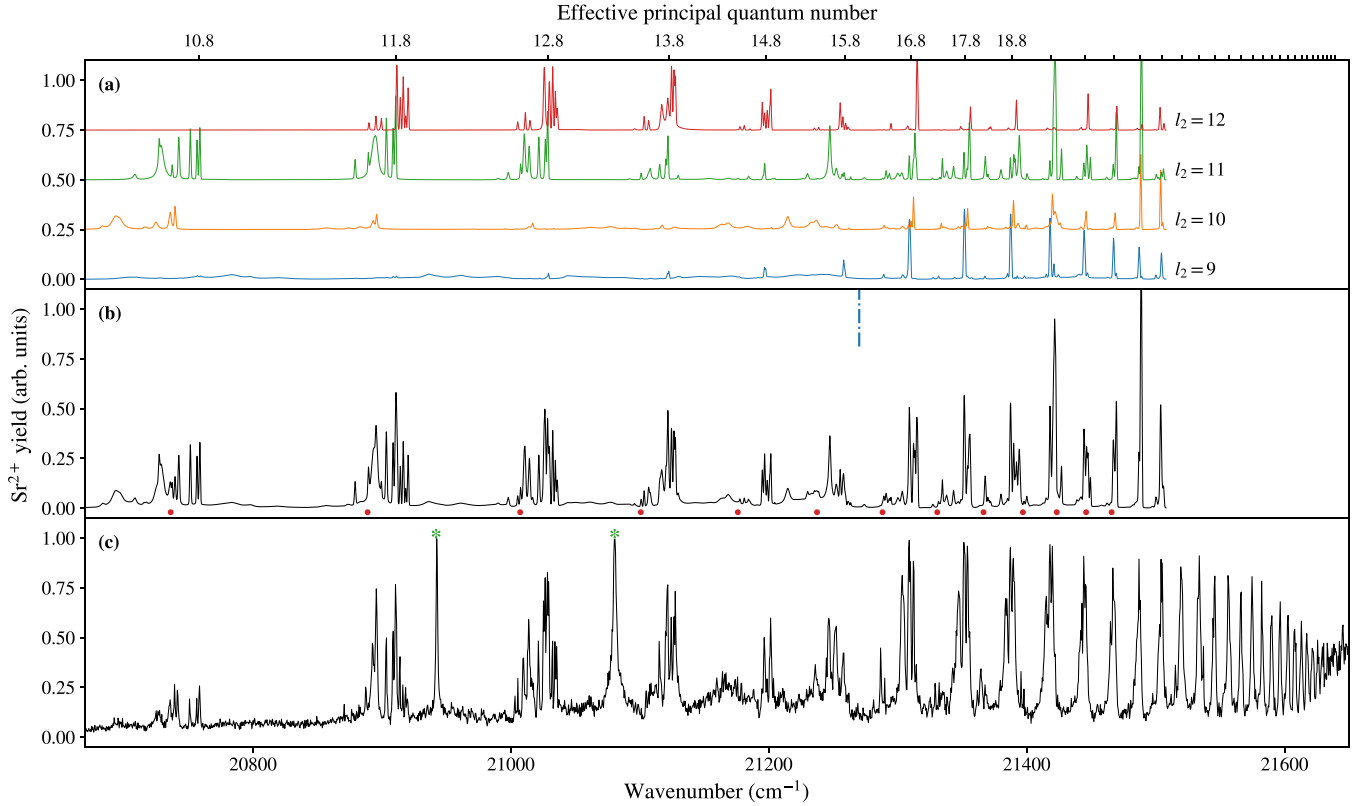


FIG. 2. Theoretical (a), (b) and experimental (c) Sr^{2+} spectra from $[5d_{5/2}16(l_2)j_2]_J$ states ($l_2 = 9-12$) in the vicinity of the $\text{Sr}^+(5d_{5/2} - 7d_{5/2})$ transition (vertical chained line). The contributions of initial states with different l_2 values to the total spectrum are shown in panel (a), where they have been offset vertically by arbitrary amounts for clarity. The asterisks in the lower panel denote the $\text{Sr}^+(6s_{1/2} - 7p_{1/2,3/2})$ resonances. Effective principal quantum numbers relative to the $\text{Sr}^+(7d_{5/2})$ threshold are shown on the upper horizontal axis. The circles in the upper panel show the position of states with effective principal quantum numbers starting from 10.8 and converging to the $\text{Sr}^+(7d_{3/2})$ threshold.

$n_1l_1j_1 - n'_1l'_1j'_1$ transition frequency of the bare Sr^+ ion, and are independent of the values of n_2 , l_2 , and j_2 . In other words, we assume that the Rydberg electron is a spectator of core excitation and does not undergo shake-up or shake-down. Under these assumptions, the relative excitation efficiencies from, first, the $[5s_{1/2}16(l_2)j_2]_{J'=l_2}$ states to the $[5p_{3/2}16(l_2)j_2]_J$ states and, second, the $[5p_{3/2}16(l_2)j_2]_J$ states to the $(5d_{5/2}16(l_2)j_2)_J$ states can be directly computed using Eq. (10). Because lasers with parallel linear polarizations were used, $M = q = 0$. The CI-ECS calculations show that the $[5d_{5/2}16(l_2)j_2]_J$ states possess in fact small nonzero quantum defects ($\mu < 0.02$) and, in particular, that for a given l_2 value the $[5d_{5/2}16(l_2)_{l_2-1/2}]_{l_2+2}$ and $[5d_{5/2}16(l_2)_{l_2+1/2}]_{l_2-2}$ states systematically lie $\approx 0.5 \text{ cm}^{-1}$ higher than the other states. The excitation-lasers detunings are thus different for the two spectrally separated groups of states, which affects the relative excitation efficiencies. In the experiment, the wavelengths of the third and fourth dye lasers driving the inner-electron transitions $5s$ to $5p_{3/2}$ and $5p_{3/2}$ to $5d_{5/2}$ were tuned to the respective ionic resonances and manually slightly adjusted to maximize the Sr^{2+} signal when all lasers were present. We empirically took this into account when calculating the theoretical spectra by visually fitting the ratio of excitation efficiencies to the two different groups of states to the experimental spectra. Optimal results were obtained when dividing

the excitation efficiencies to the $[5d_{5/2}16(l_2)_{l_2-1/2}]_{l_2+2}$ and $[5d_{5/2}16(l_2)_{l_2+1/2}]_{l_2-2}$ states by a factor of 4.

Because of nonadiabatic effects during Stark switching, the atoms are not necessarily prepared in a $6s16(l_2)$ state with a single value of l_2 . For $7p_{5/2}n'_2l'_2$ states with low n'_2 values ($n'_2 \lesssim 14$) and for $8p_{3/2}n'_2l'_2$ states around $n'_2 = 15$, the groups of lines associated with different initial l_2 values are partially resolved in the experimental spectra. We have used these lines to estimate the relative populations of the initial states with different l_2 values by visually fitting the calculated data to the experimental spectra (see, e.g., Fig. 2). We carried out calculations for a number of l_2 values and added them to obtain the total spectrum, with weights corresponding to the respective l_2 populations. The l_2 weights are summarized in the lower part of Table II.

TABLE II. Populations of the various $[5d_{5/2}16(l_2)j_2]_J$ initial states.

	$J = l_2 - 2$	$J = l_2$	$J = l_2 + 2$
$[5d_{5/2}16(l_2)_{l_2-1/2}]_J$	0.13	0.15	0.18
$[5d_{5/2}16(l_2)_{l_2+1/2}]_J$	0.16	0.16	0.21
$l_2 = 9$	$l_2 = 10$	$l_2 = 11$	$l_2 = 12$
0.44	0.4	0.08	0.08

IV. RESULTS

A. Photoionization spectra

The experimental Sr^{2+} overview spectrum we recorded is shown in Fig. 1. The regions below and above the $\text{Sr}^+(7d)$ ionization threshold are discussed separately in the following. The theoretical and experimental Sr^{2+} spectra in the first region, where $7dnl$ doubly excited states can be excited, are compared in Fig. 2. The contributions of initial states with different l_2 values are also shown. The theoretical spectrum is truncated to Rydberg states with $n \leq 24$, corresponding to the highest n value accurately described by our basis set. The spectrum was displaced along the horizontal axis by the difference between the calculated and experimental [57] wave numbers of the $\text{Sr}^+(5d_{5/2} - 7d_{5/2})$ transition (26.42 cm^{-1}). In the experiment, the l_2 , j_2 , and J substructure of the $[5d_{5/2}16(l_2)_{j_2}]_J$ initial states is not well resolved, which results in small mismatches between the photon energies of the third and fourth lasers used to prepare the various $[5d_{5/2}16(l_2)_{j_2}]_J$ states and the exact ICE energies. The resulting offset between the experimental and theoretical wave numbers for the fifth laser is estimated to be $\approx -0.8 \text{ cm}^{-1}$ overall and was corrected by shifting the theoretical spectrum along the horizontal axis accordingly. Overall, the agreement between theory and experiment is very good considering the complexity of the experiment. Discrepancies can be attributed to uncertainties in the modeling of the Sr^{2+} production (see Sec. III B), variations of the laser pulse energy or of the detection efficiency in the experiment, inaccuracies of the calculation and in particular of the model potential, missing initial states, or inaccurate initial populations. In many cases a quantitative level of agreement is reached, which is significant for such high-lying doubly excited states [41].

The spectra show a regular Rydberg-series progression, with an associated quantum defect of ≈ 0.2 , converging to the $\text{Sr}^+(7d_{5/2})$ threshold. A weaker series with approximately the same quantum defect and converging to the other spin-orbit component ($7d_{3/2}$) is marked by the circles. For singly excited Rydberg states and core-excited Rydberg states, the quantum defects of high- l Rydberg series ($l = 9-12$ in the present case) are very small. The interaction between the core and Rydberg electrons is indeed strongly reduced by the large centrifugal barrier which prevents the penetration of the Rydberg electron in the core region. Conversely, the large (≈ 0.2) quantum defects observed in the present spectra indicate much stronger correlations between the two electrons, which will be analyzed in more detail in Sec. IV B. Correlations are in fact fully responsible for the spectra shown in Fig. 2. In an ICE scheme, where electron correlations are neglected, the excitation of $[7d_{j_1}n'_2(l'_2)_{j'_2}]_J$ states from $[5d_{5/2}16(l_2)_{j_2}]_J$ states is forbidden because dipole selection rules prevent the $5d \rightarrow 7d$ core excitation. Huang *et al.* observed a similar violation of ICE predictions for higher l states ($l = 13, 15$) [11], which was also observed in CI-ECS calculations [42]. In the present case, inspection of the CI coefficients reveals that, for example, states with predominant $[7d_{5/2}n'_2(10)_{j'_2}]_J$ character are mixed at the level of 1% with $[8p_{3/2}n''_2(9, 11)_{j_2}]_J$ and $[6f_{7/2}n''_2(9, 11)_{j_2}]_J$ states. ICE to the two latter states is allowed by dipole selection rules and, because the transition dipole moment from the $5d_{5/2}$ state of Sr^+

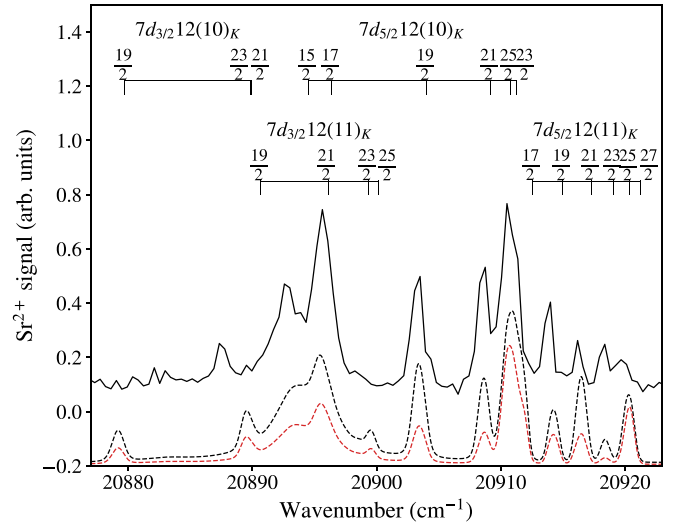


FIG. 3. Experimental (full line) and theoretical (dotted lines) Sr^{2+} spectra in the region of $7d_{3/2,5/2}12(l'_2)$ resonances. The red dotted line corresponds to a spectrum calculated from the partial photoionization cross section to states energetically higher than $\text{Sr}^+(6d)$ only, whereas the black dotted line was obtained from the total cross section. The theoretical spectra were offset by -0.2 along the vertical axis and scaled by a factor of 2 for clarity.

to the $6f_{7/2}$ state is much larger, it is the $[6f_{7/2}n''_2(9, 11)_{j_2}]_J$ character that provides the major intensity contribution to the photoexcitation spectrum.

Line intensities in the spectra show a significant decrease around $21\,250 \text{ cm}^{-1}$, a region where the principal quantum number of the outer electron is approximately conserved upon excitation ($n'_2 \sim 16$, see upper horizontal axis in Fig. 2). This fact was already observed and explained by Huang *et al.* [11]. If we consider an initial state described by a single configuration $[5d_{5/2}16(l_2)_{j_2}]_J$, the largest contributions to the transition dipole moments to $[7d_{5/2}16(l'_2)_{j'_2}]_J$ states come from the mixing of the latter states with configurations in which the Rydberg electron is in the same configuration as the initial state but the core-electron configuration has changed, e.g., $[6f_{7/2}16(l_2)_{j_2}]_J$ or $[8p_{3/2}16(l_2)_{j_2}]_J$. If one assumes that the Rydberg electron is well described by a hydrogenic wave function, a rather good approximation for high- l_2 states, then electrostatic interactions coupling the two configurations vanish for $n_2 = n'_2 = 16$ [58]. This means that, in first approximation, the $[7d_{5/2}16(l'_2)_{j'_2}]_J$ states possess only little $[6f_{7/2}16(l_2)_{j_2}]_J$ or $[8p_{3/2}16(l_2)_{j_2}]_J$ character and thus cannot be efficiently excited. This is no longer the case for noninteger values of n_2 and n'_2 or $n_2 \neq n'_2$, which explains why the line intensities do not completely vanish around $n'_2 \sim 16$ and why lines away from the $n'_2 \sim 16$ region are more intense.

Each n'_2 band in the spectra possesses a complex substructure. A detailed view of the $n'_2 \sim 12$ region is shown in Fig. 3. The agreement between theory (black dotted line) and experiment (full line) is very good and permits the assignment of each line to one or a few states with predominant $[7d_{j_1}12(10-11)_{j_2}]_J$ character. The spin-orbit interaction for the Rydberg electron is very small and levels with different j'_2 values but identical quantum numbers otherwise are

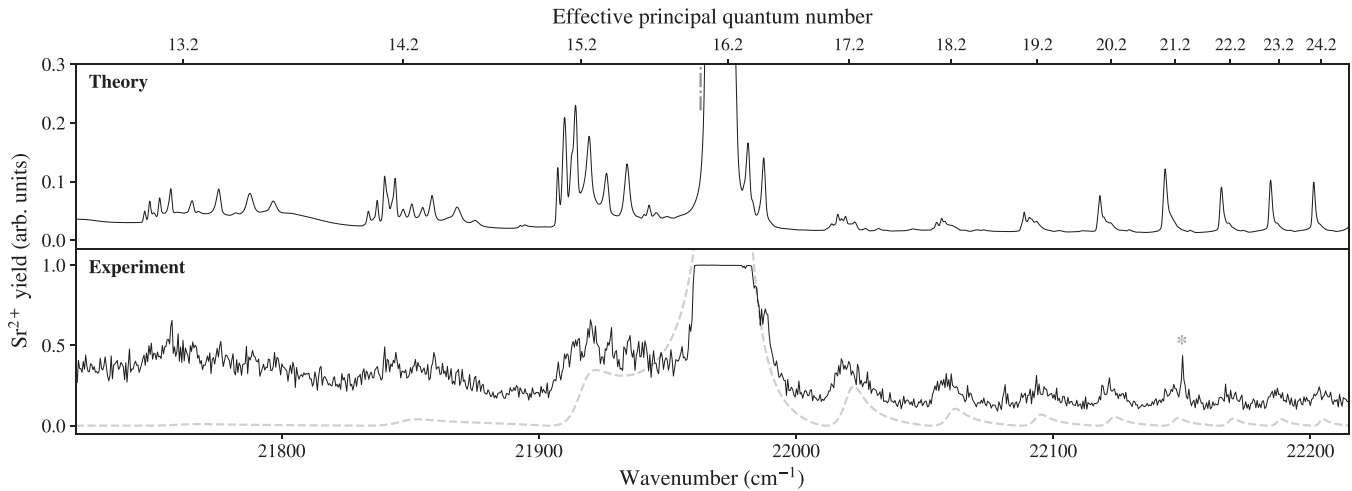


FIG. 4. Theoretical (top) and experimental (bottom) Sr^{2+} spectra from $[5d_{5/2}16(l_2)_{j_2}]_J$ states ($l_2 = 9-12$) in the vicinity of the $\text{Sr}^+(5d_{5/2} - 8p_{3/2})$ transition. The vertical chained line in the upper panel shows the position of the $\text{Sr}^+(5d_{5/2} - 8p_{3/2})$ transition. The asterisk in the lower panel denotes the $\text{Sr}^+(5p_{3/2} - 7p_{3/2})$ two-photon resonance. Effective principal quantum numbers relative to the $\text{Sr}^+(8p_{3/2})$ threshold are shown on the upper horizontal axis. The dashed gray line in the lower panel shows a typical prediction of the ICE model.

degenerate on the scale of the figure. Therefore, states were labeled in jK coupling using Eq. (3), as shown by the assignment bars. States with $l_2' = 9$ are broad and do not yield clear spectral features in the spectrum.

The theoretical and experimental Sr^{2+} spectra recorded from $[5d_{5/2}16(l_2)_{j_2}]_J$ states and for photon energies above the $\text{Sr}^+(7d)$ threshold, a region where $8pnl$ doubly excited Rydberg states are excited, are compared in Fig. 4. As for the $7dnl$ region, the theoretical spectrum was displaced along the horizontal axis by the difference between the calculated and experimental wave numbers of the $\text{Sr}^+(5d_{5/2} - 8p_{3/2})$ transition (22.0 cm^{-1} , see paragraph below) and by an additional -0.8 cm^{-1} . Agreement between theory and experiment is satisfactory. The line positions are well reproduced by theory, however lines tend to be broader in the experimental spectrum. This may be caused by inaccuracies of the model potential, by the truncation of the basis set, or by the fact that initial states with lower l_2 values are populated by nonadiabatic effects in the experiment. The latter possibility would result in $8pnl_2'$ states with lower l_2' values being excited, which possess larger autoionization rates and would give rise to broader spectral lines. The peak corresponding to an effective principal quantum number of $n_2' \sim 16.2$ is heavily saturated under the present experimental conditions.

Rydberg series with a negative quantum defect of ≈ -0.2 are observed in Fig. 4 and converge to the $\text{Sr}^+(8p_{3/2})$ threshold. The position of this threshold obtained by extrapolation of the Rydberg formula to $n \rightarrow \infty$ is $75\,335.7(7) \text{ cm}^{-1}$ relative to $\text{Sr}^+(5s)$, a value 23.9 cm^{-1} higher than the reference data from NIST [57]. Discrepancies of similar magnitudes were observed earlier by Lange *et al.* for $\text{Sr}^+(7p_{1/2,3/2})$ [59]. We therefore used, in the present paper, the value determined from our spectra.

The rich substructure of the $n_2' \sim 15$ band is shown in Fig. 5. Agreement between theory and experiment is very good and allows us to assign each peak to one or a few $[8p_{3/2}15(9-12)_{j_2}]_J$ states. As for the $7d12l_2'$ region, the spin-orbit splitting of the Rydberg electron is negligible and

states were labeled in jK coupling. The energy differences between different K states of a given l_2' manifold are large, and in fact often larger than the energy difference between states belonging to different l_2' manifolds. Thus, l_2' is no longer even an approximately good quantum number. Inspection of the CI coefficients shows that, for example, states with predominant $8p_{3/2}15(l_2' = 9)$ character are mixed with states with $l_2' = 7, 10, 11$, and 12 and core configurations $7d_{3/2,5/2}$, $8p_{1/2}$, and $6(5)_{9/2,11/2}$.

The signal computed from the partial photoionization cross section to $\text{Sr}^+(7d_{3/2,5/2})$ states *only* is shown by the dotted red line in Fig. 5, and appears very similar to the signal

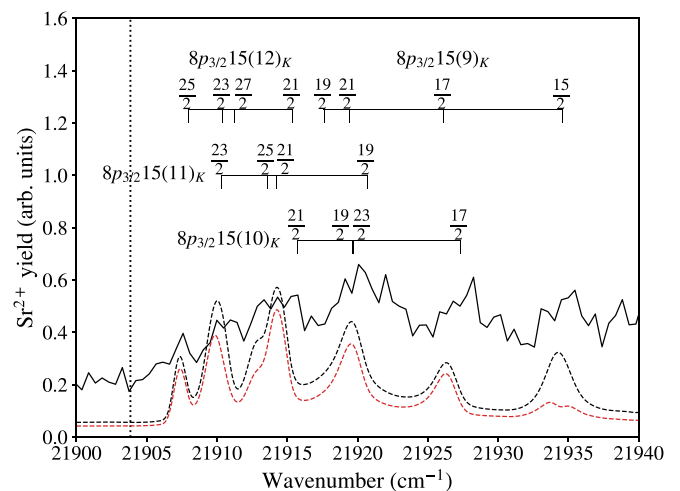


FIG. 5. Experimental (full line) and theoretical (dotted lines) Sr^{2+} spectra in the region of $8p_{3/2}15(l_2')$ resonances. The red dotted line corresponds to the signal calculated from the partial photoionization cross section to the $\text{Sr}^+(7d)$ states only, whereas the black dotted line was obtained from the total cross section. The vertical dotted line indicates the position of a $8p_{3/2}15(l_2')$ state with zero quantum defect. The theoretical spectra were scaled by a factor of 3 for clarity.

calculated from the total cross section (black dotted line). Therefore, the doubly excited $8p_{3/2}15(l_2)_K$ states autoionize predominantly into $7d\epsilon l$ continua. The kinetic energy ϵ of the ejected electron is relatively small because the $8p_{3/2}15(l_2)_K$ states are energetically close to the $\text{Sr}^+(7d_{3/2,5/2})$ thresholds ($\approx 200 \text{ cm}^{-1}$). In contrast, autoionization of the $7dnl$ states observed in Fig. 2 yields higher electron energies because these states are more than 4000 cm^{-1} higher than the closest-lying $\text{Sr}^+(7p, 5f)$ thresholds. Autoionization typically becomes less efficient the larger the momentum transfer between the Rydberg and core electrons [24,44], which translates into the fact that, as observed in the spectra, the overall widths of $7dnl$ states are narrower than the $8pnl$ ones.

Let us now investigate the intensity distribution of the lines in the spectra shown in Fig. 4. In contrast with the $7dnl$ region shown in Fig. 2, ICE from the $5d_{5/2}$ state to the $8p_{3/2}$ state is allowed by dipole selection rules. We calculated the typical predictions of the independent-electron ICE model [7,56] considering an isolated Rydberg series with a quantum defect of -0.21 and linewidths given by $50 \times 10^3/n^3 \text{ cm}^{-1}$, as shown by the dashed gray line in the lower panel of Fig. 4. The strongest transition around 21970 cm^{-1} corresponds to the situation where the principal quantum number of the outer electron is approximately conserved upon photoexcitation ($n_2 \sim n_1 \sim 16$). Shake-up and shake-down of the outer electron are possible and the intensity of the corresponding satellite lines decreases following the sinc^2 law in Eq. (11). The ICE model reproduces the overall intensity behavior of the spectrum, however closer inspection reveals that the lines in the theoretical and experimental spectra do not decay as rapidly as the ICE predictions, in particular in the low-wave-number side. It is possible that such a discrepancy is caused by variations of the laser pulse energy with the wave number or changes in the detection efficiency with the principal quantum number of the Rydberg electron. However, the low-wave-number region also corresponds to low principal quantum numbers of the outer electron, where the strongest correlations with the core electron are expected and thus where the largest deviations from ICE should occur. The continuous background in the experimental and theoretical spectra is not reproduced by the ICE model and corresponds to direct ionization into $7d\epsilon l$ continua. It is in fact the continuation of the Rydberg series observed in Fig. 2 to positive electron energies.

B. Electronic correlations

Electron correlations responsible for the complex structures observed in the experimental and theoretical spectra presented above can be investigated in their full extent with the aid of the two-electron density $\rho(r_1, r_2, \theta_{12})$, calculated from the CI-ECS wave functions as described in Sec. III. We will focus in the following on the $[7d_{5/2}12(10)j_2]_J'$ and $[8p_{3/2}13(11)j_2]_J'$ states, however we verified that similar conclusions apply to other states as well.

Let us first investigate radial correlations. To do so, we integrate the three-dimensional two-electron density over the angular coordinate $\cos \theta_{12}$:

$$\tilde{\rho}(r_1, r_2) = \int d(\cos \theta_{12}) \rho(r_1, r_2, \cos \theta_{12}). \quad (12)$$

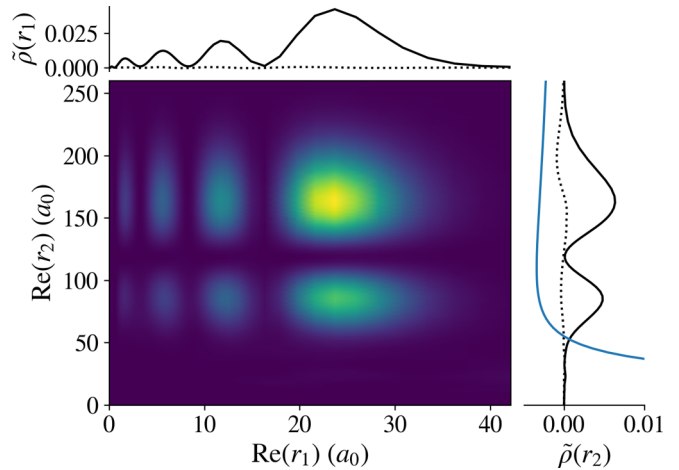


FIG. 6. Radial electronic density $\rho(r_1, r_2)$ of the $[7d_{5/2}12(10)_{21/2}]_8$ state. Radial densities integrated over r_2 and r_1 are shown in the top and right panels, respectively. The blue line in the right panel shows the sum of a Coulomb potential and a centrifugal potential for $l = 10$.

It yields the radial density shown in Fig. 6 for the $[7d_{5/2}12(10)_{21/2}]_8$ state, which is associated with a K value of $15/2$ in jK coupling. Further integration over r_1 yields the one-dimensional density the real (full line) and imaginary (dotted line) parts of which are shown in the right panel. Integration over r_2 gives the density shown in the top panel. The blue line in the right panel shows the sum of a pure Coulomb potential and a centrifugal potential for $l = 10$. Complex rotation is applied from $r_{1,2} = 150 a_0$ onward, at which point the densities calculated from the CI-ECS wave functions do not necessarily follow the usual probabilistic meaning of Hermitian quantum mechanics. Due to exchange symmetry, $\tilde{\rho}(r_1, r_2)$ presents the same behavior for r_1 and r_2 reversed. This is not shown for clarity.

The radial density in Fig. 6 reveals that radial electronic correlations [60] are weak. Indeed, the total density is essentially the product of two independent one-electron densities: one associated with the outer electron density, which resembles the norm squared of the radial function of a $n = 12$, $l = 10$ Rydberg electron; the other associated with the density of the core electron, which resembles the norm squared of the $\text{Sr}^+(7d_{5/2})$ wave function. The absence of radial correlations is not surprising since the two electrons occupy largely different regions of the radial phase space. As shown in the right panel of Fig. 6, the radial density associated with the outer electron is confined to $r \gtrsim 50 a_0$ by the large centrifugal barrier it experiences, whereas the inner electron density vanishes at $r \sim 40 a_0$ and beyond.

Angular correlations [60], on the other hand, are far from negligible. Figure 7(a) shows the conditional density of the core electron when the outer electron is fixed at $r_2 = 85 a_0$, corresponding to the first maximum of the outer-electron distribution in the right panel of Fig. 6. One notices that the inner electron preferentially sits at $\theta_{12} = 180^\circ$, i.e., on the side of the nucleus opposite to the outer electron. Comparison with the conditional density calculated using the independent-electron approximation, shown in Fig. 7(b), reveals that the

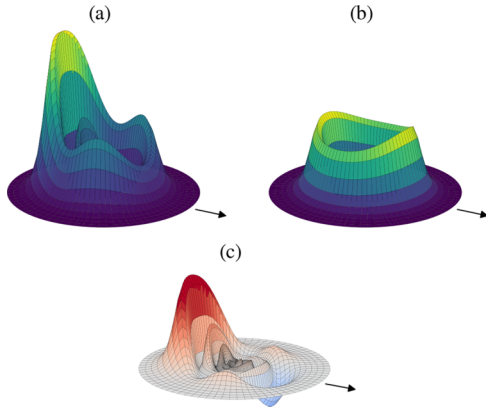


FIG. 7. Conditional density $\rho(r_1, \theta_{12}|r_2 = 85a_0)$ of the $[7d12(10)_{21/2}]_8$ state in the presence (a) and absence (b) of electron correlations. Panel (c) shows the difference between the two densities. The black arrow shows the direction along which $\theta_{12} = 0^\circ$.

strong polarization of the core-electron density is caused by its interaction with the outer electron. In order to make correlation-induced changes in the core-electron density more apparent, we also calculated the difference between the conditional densities with [Fig. 7(a)] and without [Fig. 7(b)] correlations, as shown in Fig. 7(c).

The differences between the conditional densities $\rho(r_1, \theta_{12}|r_2 = 85 a_0)$ with and without correlations are shown in Fig. 8 for the various $7d_{5/2}12(10)_K$ states. In all cases, the inner-electron density is significantly distorted by

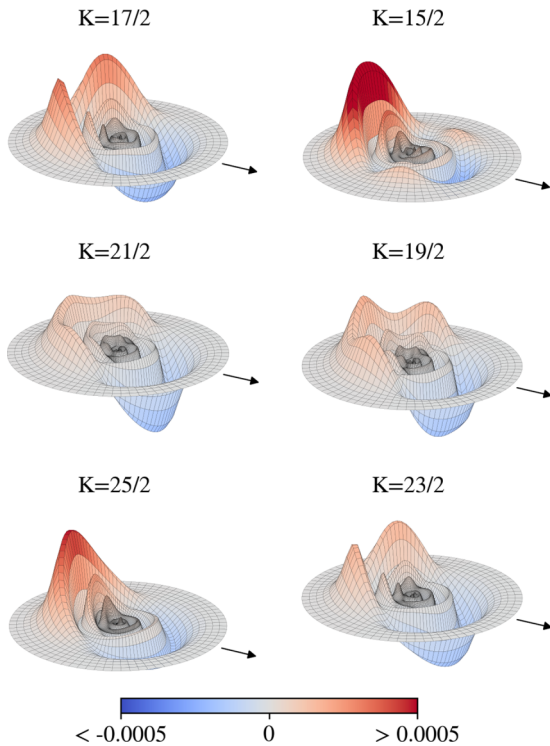


FIG. 8. Difference between the conditional probability densities $\rho(r_1, \theta_{12}|r_2 = 85a_0)$ with and without electronic correlations for the various $7d_{5/2}12(10)_K$ states. The black arrow shows the direction along which $\theta_{12} = 0^\circ$.

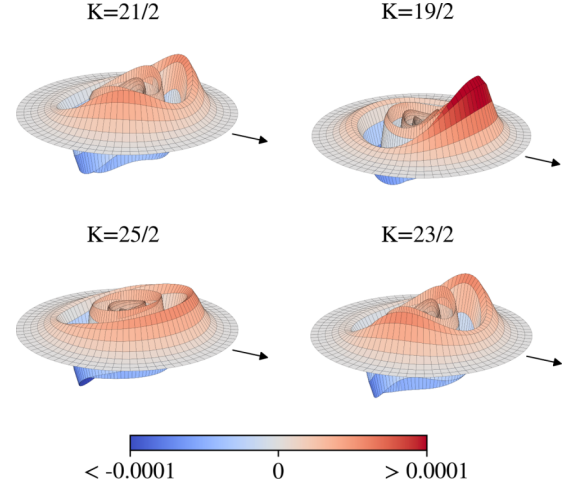


FIG. 9. Difference between the conditional probability densities $\rho(r_1, \theta_{12}|r_2 = 120 a_0)$ with and without electronic correlations for the various $8p_{3/2}13(11)_K$ states. The black arrow shows the direction along which $\theta_{12} = 0^\circ$.

its interaction with the outer electron. The densities for the different K values can be grouped in three categories with $K = 15/2$ and $25/2$, $K = 17/2$ and $23/2$, and $K = 19/2$ and $21/2$, respectively. They are characterized by the presence of zero, one, and two minima in the conditional density along the θ_{12} direction in the $[\frac{\pi}{2}, -\frac{\pi}{2}]$ half plane, respectively. In the limit where the radial motion of the outer electron can be adiabatically decoupled from that of the inner electron, these three categories correspond to different projections of the total orbital angular momentum of the core electron onto an adiabatic quantization axis defined by the distance between the nucleus and the outer electron (r_2).

Figure 9 shows the differences between the conditional densities $\rho(r_1, \theta_{12}|r_2 = 120 a_0)$ with and without correlations for the various $8p_{3/2}13(11)_K$ states. Contrary to the $7d_{5/2}12(10)_K$ states, the core-electron density is polarized toward $\theta_{12} = 0^\circ$, as is particularly visible for $K = 19/2$. The inner electron thus preferentially resides on the same side of the nucleus as the outer electron. The densities can be grouped into $K = 19/2$ and $25/2$, and $K = 21/2$ and $23/2$, characterized by the presence of zero and one minima along the θ_{12} direction in the $[-\frac{\pi}{2}, \frac{\pi}{2}]$ half plane, respectively.

V. DISCUSSION

Because the effective principal quantum number of the outer electron is significantly larger than that of the inner one, the classical orbit period of the former is much larger than the one of the latter ($n_2^3 \gg n_1^3/4$). The precession of the Runge-Lenz vector, which is classically equivalent to the precession of the major axis associated to the elliptic orbit of the inner electron, is also much faster than the classical orbit period of the outer electron because [10]

$$n_2^3 \gg \frac{n_1^3}{4} \left(\frac{\partial \mu_{l_1}(E)}{\partial l_1} \right)^{-1}, \quad (13)$$

where $\mu_{l_1}(E)$ represents the quantum defects of $\text{Sr}^+(n_1 l_1)$ orbitals at energy E . Thus, in first approximation, the

radial motion of the outer electron can be adiabatically decoupled from the motion of the inner electron (see, e.g., Refs. [31,33,61]). Such a procedure is further supported by the absence of strong radial correlations in the CI-ECS two-electron densities. Within the adiabatic picture, the inner electron evolves in the static electric field generated by the outer electron, which is fixed at a given point r_2 in space. This approach is equivalent to the clamped-nuclei approximation in molecular physics, and offers a qualitative understanding of the quantum defects and charge densities presented above.

In the Sr^+ ion, the scalar polarizability of the $7d_{5/2}$ orbital, calculated using the one-electron radial functions of Sec. III A, is $\alpha_0 \sim 54\,332\,a_0^3$. Thus, the $\text{Sr}^+(7d_{5/2})$ state is redshifted by its interaction with an external electric field and the charge distribution localizes preferentially on the side of the nucleus opposite to the electric-field direction. In the present case, this translates into the core electron sitting preferentially on the side of the nucleus opposite to the outer electron. Conversely, the scalar polarizability of $\text{Sr}^+(8p_{3/2})$ is $\alpha_0 \sim -58\,794\,a_0^3$. It is blueshifted by an external electric field and the center of gravity of the charge distribution is displaced away from the nucleus in the direction of the electric field. The inner electron preferentially resides on the same side of the nucleus as the outer electron. The fact that the polarizabilities of $\text{Sr}^+(7d_{5/2})$ and $\text{Sr}^+(8p_{3/2})$ have similar magnitudes but different signs further explains why $7p_{5/2}nl$ and $8p_{3/2}nl$ doubly excited states exhibit quantum defects of similar magnitude but opposite signs. For $7d_{5/2}(n'_2 = 12, l'_2 = 10)$ states, the electric field generated by the outer electron at its mean radial distance induces an energy shift due to the scalar polarizability of the ion core of $\approx -31\text{ cm}^{-1}$, comparable to the shift observed in the experimental spectrum. For $8p_{3/2}(n'_2 = 15, l'_2 = 11)$ states, the shift is $\approx 12\text{ cm}^{-1}$, which compares well with observations (see Fig. 5). Energy shifts depending on the projection of the total angular momentum of the inner electron onto the adiabatic quantization axis (r_2) can in principle be derived by taking into account the tensor polarizability (α_2) of the Sr^+ orbital under consideration [62]. However, the agreement with the observed and calculated energies is not significantly improved, a fact we attribute primarily to nonadiabatic effects not accounted for in our simple model.

The doubly excited states under scrutiny are called planetary states [4,9,10,15], by analogy with planets in a solar system. The autoionization lifetimes we calculate for these states are long [$\approx 10^{-12}$ – 10^{-10} s for $7d_{5/2}12(10)$ states] compared to the classical orbit period of the Rydberg electron ($\tau \sim 40$ fs for $n = 12$). The planetary system is thus metastable and survives for a large number of orbits. The two electrons describe a synchronous angular motion the details of which depend primarily on the polarizability of the ion core and the projection of the ion-core total angular momentum onto the adiabatic outer-electron-nucleus axis. For the $7dnl$ and $8pnl$ states considered in the present paper, the two electrons are preferentially either at 0° or 180° from each other depending on the sign of the static polarizability of the ion core. However, their radial motion is not constrained and they are free to roam along the electron-nucleus-electron direction. This differs from the frozen-planet states calculated by Richter and Wintgen for low angular momentum, high-lying doubly

excited states of helium [5,33], in which the two electrons are further localized at specific r_1 and r_2 values on the radial axis due to strong radial correlations.

VI. CONCLUSION

We presented an experimental and theoretical study of $7dnl$ and $8pnl$ planetary states of Sr. Experimental spectra were recorded by photoexcitation from $5dnl$ states, prepared by multiphoton excitation of ground-state atoms and using the Stark-switching technique, followed by double ionization *via* autoionization, photoionization, field ionization, and any combination thereof. Theoretical spectra were calculated using the method of configuration interaction with exterior complex scaling, which permitted the complete treatment of the dynamics of the two highly excited electrons from first principles. Good agreement was obtained with experimental data, and permitted the detailed analysis of the complex structures observed in the spectra. The signatures of electron-electron correlations in the spectra were carefully investigated. Electronic correlations were further investigated using two-electron conditional probability densities calculated from CI-ECS wave functions. A strong distortion of the inner-electron density caused by its interaction with the outer electron was observed, and was related to the polarization of the ion core by the electric field of the outer electron and to the orientation of the ion-core angular momentum relative to the nucleus-outer-electron adiabatic axis. The present paper thus validates, through calculations from first principles in quantitative agreement with high-resolution experimental results, the frozen-planet approximation that describes qualitatively the structure of planetary states based on the polarization of the inner electron by the Rydberg electron [9,10,17,27,31]. Similar ideas were developed in the early days of quantum mechanics [63,64] and are being used, e.g., to study high- l singly excited Rydberg series of K [65]. In doubly excited Rydberg states, core-polarization effects are dramatically enhanced compared to singly excited Rydberg states because static polarizabilities scale as n^7 [66]. We further see that quantitative agreement between calculated and measured energy levels can only be reached through complete calculations taking into account higher-order electrostatic interactions and nonadiabatic effects.

For larger orbital momenta l_1 of the inner electron, the ion core is expected to be more polarizable and the dynamics described in the present paper should be yet more pronounced. Such states are for example the $6gnl$ or $6hnl$ states lying energetically just above the $8pnl$ states we studied. Moreover, because the quantum defects μ_{l_1} associated with high l_1 values are small, Eq. (13) should be violated for values of the principal quantum number n_2 of the outer electron that are accessible to both theory and experiment. The study of such states is a perspective of future work as it would provide further information on the dynamics of planetary states. It would also allow one to track the progressive breakdown of the frozen-planet approximation as, for decreasing n_2 values, the motion of the outer electron can no longer be adiabatically separated from the motion of the inner electron and radial correlations become more pronounced. Another perspective is the study of states where the centrifugal barrier associated

with the outer electron is small enough to allow its penetration in the core region. Frozen-planet states [5], exhibiting strong radial *and* angular correlations, are known to form under such conditions in the He atom but their existence in other systems remains elusive.

ACKNOWLEDGMENTS

The authors gratefully acknowledge fruitful discussions with F. Merkt and D. Wehrli, and W. Huang for his help with the experiment at an early stage of this work.

- [1] M. Aymar, C. H. Greene, and E. Luc-Koenig, *Rev. Mod. Phys.* **68**, 1015 (1996).
- [2] G. Tanner, K. Richter, and J. M. Rost, *Rev. Mod. Phys.* **72**, 497 (2000).
- [3] K. Richter, G. Tanner, and D. Wintgen, *Phys. Rev. A* **48**, 4182 (1993).
- [4] P. Camus, *Phys. Scr. T* **51**, 20 (1994).
- [5] K. Richter and D. Wintgen, *J. Phys. B* **24**, L565 (1991).
- [6] R. P. Madden and K. Codling, *Phys. Rev. Lett.* **10**, 516 (1963).
- [7] W. E. Cooke, T. F. Gallagher, S. A. Edelstein, and R. M. Hill, *Phys. Rev. Lett.* **40**, 178 (1978).
- [8] E. Y. Xu, Y. Zhu, O. C. Mullins, and T. F. Gallagher, *Phys. Rev. A* **35**, 1138 (1987).
- [9] U. Eichmann, V. Lange, and W. Sandner, *Phys. Rev. Lett.* **64**, 274 (1990).
- [10] U. Eichmann, V. Lange, and W. Sandner, *Phys. Rev. Lett.* **68**, 21 (1992).
- [11] W. Huang, C. Rosen, U. Eichmann, and W. Sandner, *Phys. Rev. A* **61**, 040502(R) (2000).
- [12] S. Cohen, M. Aymar, A. Bolovinos, M. Kompitsas, E. Luc-Koenig, H. Mereu, and P. Tsekeris, *Eur. Phys. J. D* **13**, 165 (2001).
- [13] U. Eichmann, T. F. Gallagher, and R. M. Konik, *Phys. Rev. Lett.* **90**, 233004 (2003).
- [14] G. Fields, X. Zhang, F. B. Dunning, S. Yoshida, and J. Burgdörfer, *Phys. Rev. A* **97**, 013429 (2018).
- [15] I. C. Percival, *Proc. R. Soc. A* **353**, 289 (1977).
- [16] P. Camus, S. Cohen, L. Pruvost, and A. Bolovinos, *Phys. Rev. A* **48**, R9 (1993).
- [17] R. R. Jones and T. F. Gallagher, *Phys. Rev. A* **42**, 2655 (1990).
- [18] S. N. Pisharody and R. R. Jones, *Science* **303**, 813 (2004).
- [19] M. Aymar, E. Luc-Koenig, and S. Watanabe, *J. Phys. B* **20**, 4325 (1987).
- [20] J. Millen, G. Lochead, and M. P. A. Jones, *Phys. Rev. Lett.* **105**, 213004 (2010).
- [21] R. Mukherjee, J. Millen, R. Nath, M. P. A. Jones, and T. Pohl, *J. Phys. B* **44**, 184010 (2011).
- [22] R. C. Teixeira, A. Larrouy, A. Muni, L. Lachaud, J.-M. Raimond, S. Gleyzes, and M. Brune, *Phys. Rev. Lett.* **125**, 263001 (2020).
- [23] I. S. Madjarov, J. P. Covey, A. L. Shaw, J. Choi, A. Kale, A. Cooper, H. Pichler, V. Schkolnik, J. R. Williams, and M. Endres, *Nat. Phys.* **16**, 857 (2020).
- [24] H. Lehec, X. Hua, P. Pillet, and P. Cheinet, *Phys. Rev. A* **103**, 022806 (2021).
- [25] D. Wehrli, M. Génévriez, and F. Merkt, *Phys. Rev. A* **100**, 012515 (2019).
- [26] J. Wilson, S. Saskin, Y. Meng, S. Ma, R. Dilip, A. Burgers, and J. Thompson, [arXiv:1912.08754v2](https://arxiv.org/abs/1912.08754v2) (2019).
- [27] P. Camus, T. F. Gallagher, J. M. Lecomte, P. Pillet, L. Pruvost, and J. Boulmer, *Phys. Rev. Lett.* **62**, 2365 (1989).
- [28] K. Codling, *Nature (London)* **344**, 194 (1990).
- [29] V. N. Ostrovsky, *J. Phys. B* **26**, 1163 (1993).
- [30] W. Huang, X. Y. Xu, C. B. Xu, M. Xue, L. Q. Li, and D. Y. Chen, *Phys. Rev. A* **49**, R653(R) (1994).
- [31] K. D. Heber, M. Seng, M. Halka, U. Eichmann, and W. Sandner, *Phys. Rev. A* **56**, 1255 (1997).
- [32] M. Domke, C. Xue, A. Puschmann, T. Mandel, E. Hudson, D. A. Shirley, G. Kaendl, C. H. Greene, H. R. Sadeghpour, and H. Petersen, *Phys. Rev. Lett.* **66**, 1306 (1991).
- [33] K. Richter, J. S. Briggs, D. Wintgen, and E. A. Solov'ev, *J. Phys. B* **25**, 3929 (1992).
- [34] A. Bürgers, D. Wintgen, and J.-M. Rost, *J. Phys. B* **28**, 3163 (1995).
- [35] A. Czasch, M. Schöffler, M. Hattass, S. Schössler, T. Jahnke, T. Weber, A. Staudte, J. Titze, C. Wimmer, S. Kammer, M. Weckenbrock, S. Voss, R. E. Grisenti, O. Jagutzki, L. P. H. Schmidt, H. Schmidt-Böcking, R. Dörner, J. M. Rost, T. Schneider, C.-N. Liu *et al.*, *Phys. Rev. Lett.* **95**, 243003 (2005).
- [36] J. Eiglsperger, B. Piraux, and J. Madroñero, *Phys. Rev. A* **80**, 022511 (2009).
- [37] J. Madroñero and A. Buchleitner, *Phys. Rev. A* **77**, 053402 (2008).
- [38] A. González-Melan and J. Madroñero, *Phys. Rev. A* **101**, 013414 (2020).
- [39] T. P. Grozdanov, A. A. Gusev, E. A. Solov'ev, and S. I. Vinitzky, *Eur. Phys. J. D* **74**, 161 (2020).
- [40] Y. Wang and C. H. Greene, *Phys. Rev. A* **103**, 033103 (2021).
- [41] R. P. Wood and C. H. Greene, *Phys. Rev. A* **49**, 1029 (1994).
- [42] M. Génévriez, *Mol. Phys.* **119**, e1861353 (2021).
- [43] R. R. Freeman and D. Kleppner, *Phys. Rev. A* **14**, 1614 (1976).
- [44] M. Génévriez, D. Wehrli, and F. Merkt, *Phys. Rev. A* **100**, 032517 (2019).
- [45] B. Simon, *Phys. Lett. A* **71**, 211 (1979).
- [46] T. N. Rescigno and C. W. McCurdy, *Phys. Rev. A* **62**, 032706 (2000).
- [47] R. D. Cowan, *The Theory of Atomic Structure and Spectra*, Los Alamos Series in Basic and Applied Sciences (University of California, Berkeley, 1981).
- [48] T. N. Rescigno and V. McKoy, *Phys. Rev. A* **12**, 522 (1975).
- [49] T. Carette, J. M. Dahlström, L. Argenti, and E. Lindroth, *Phys. Rev. A* **87**, 023420 (2013).
- [50] A. Mihelič, *Phys. Rev. A* **98**, 023409 (2018).
- [51] G. S. Ezra and R. S. Berry, *Phys. Rev. A* **28**, 1974 (1983).
- [52] A. Buchleitner, B. Grémaud, and D. Delande, *J. Phys. B* **27**, 2663 (1994).
- [53] J. W. Warner, L. S. Bartell, and S. M. Blinder, *Int. J. Quantum Chem.* **18**, 921 (1980).
- [54] C. Rosen, M. Dörr, U. Eichmann, and W. Sandner, *Phys. Rev. Lett.* **83**, 4514 (1999).
- [55] P. Antoine, N.-E. Essarroukh, J. Jureta, X. Urbain, and F. Brouillard, *J. Phys. B* **29**, 5367 (1996).

- [56] S. A. Bhatti, C. L. Cromer, and W. E. Cooke, *Phys. Rev. A* **24**, 161 (1981).
- [57] A. Kramida, Y. Ralchenko, and J. Reader, NIST Atomic Spectra Database, version 5.8 (2020), <https://www.nist.gov/pml/atomic-spectra-database>.
- [58] S. Pasternack and R. M. Sternheimer, *J. Math. Phys.* **3**, 1280 (1962).
- [59] V. Lange, M. A. Khan, U. Eichmann, and W. Sandner, *Z. Phys. D* **18**, 319 (1991).
- [60] U. Fano, *Rep. Prog. Phys.* **46**, 97 (1983).
- [61] V. N. Ostrovsky and N. V. Prudov, *J. Phys. B* **28**, 4435 (1995).
- [62] J. Mitroy, M. S. Safronova, and C. W. Clark, *J. Phys. B* **43**, 202001 (2010).
- [63] J. E. Mayer and M. G. Mayer, *Phys. Rev.* **43**, 605 (1933).
- [64] M. Born and W. Heisenberg, *Z. Phys.* **23**, 388 (1924).
- [65] M. Peper, F. Helmrich, J. Butscher, J. A. Agner, H. Schmutz, F. Merkt, and J. Deiglmayr, *Phys. Rev. A* **100**, 012501 (2019).
- [66] T. F. Gallagher, *Rydberg Atoms* (Cambridge University, Cambridge, England, 1994).